Nat Nanotechnol. Author manuscript; available in PMC 2015 July 01.

Published in final edited form as:

Nat Nanotechnol. 2015 January ; 10(1): 60–64. doi:10.1038/nnano.2014.262.

Nanoscale stiffness topography reveals structure and mechanics of the transport barrier in intact nuclear pore complexes

Aizhan Bestembayeva[#1,2], **Armin Kramer**[#1,3], **Aksana A. Labokha**[4,†], **Dino Osmanović**[1,2], **Ivan Liashkovich**[3], **Elena V. Orlova**[5], **Ian J. Ford**[1,2], **Guillaume Charras**[1,6], **Ariberto Fassati**[4,‡], and **Bart W. Hoogenboom**[1,2,‡]

[1]London Centre for Nanotechnology, University College London, 17-19 Gordon Street, London WC1H 0AH, United Kingdom

[2]Department of Physics and Astronomy, University College London, Gower Street, London WC1E 6BT, United Kingdom

[3]Institute of Physiology II, University of Münster, Robert-Koch Strasse 27b, 48149 Münster, Germany

[4]Wohl Virion Centre, Division of Infection & Immunity, MRC Centre for Medical Molecular Virology, University College London, Gower Street, London WC1E 6BT, United Kingdom

[5]Department of Biological Sciences, Birkbeck College, Institute of Structural and Molecular Biology, Malet Street, London WC1E 7HX, United Kingdom

[6]Department of Cell and Developmental Biology, University College London, Gower Street, London WC1E 6BT, United Kingdom

[#] These authors contributed equally to this work.

Abstract

The nuclear pore complex (NPC) is the gate for transport between the cell nucleus and the cytoplasm. Small molecules cross the NPC by passive diffusion, but molecules larger than ~5 nm must bind to nuclear transport receptors to overcome a selective barrier within the NPC[1]. Whilst the structure and shape of the cytoplasmic ring of the NPC are relatively well characterized[2-5], the selective barrier is situated deep within the central channel of the NPC and depends critically on unstructured nuclear pore proteins[5,6], and is therefore not well understood. Here, we show that stiffness topography[7] with sharp atomic force microscopy tips can generate nanoscale cross sections of the NPC. The cross sections reveal two distinct structures, a cytoplasmic ring and a central plug structure, which are consistent with the three-dimensional NPC structure derived from

[‡]Correspondence and requests for materials should be addressed to A.F. (a.fassati@ucl.ac.uk) and B.W.H. (b.hoogenboom@ucl.ac.uk).

[†]Present address: MedImmune, Granta Park, Cambridge CB21 6GH, United Kingdom

Author Contributions A.B., A.K., A.L., I.L., G.C., A.F. and B.W.H. designed the experiments. A.B., A.K., A.L. and I.L. performed the experiments. A.B., A.K., and B.W.H., with support from E.V.O., performed the data analysis. D.O., I.J.F. and B.W.H. designed and performed the polymer modelling. A.F. and B.W.H. wrote the manuscript. All authors read and commented on the manuscript.

Author Information

The authors declare no competing financial interests.

Europe PMC Funders Author Manuscripts

electron microscopy[2-5]. The central plug persists after reactivation of the transport cycle and resultant cargo release, indicating that the plug is an intrinsic part of the NPC barrier. Added nuclear transport receptors accumulate on the intact transport barrier and lead to a homogenization of the barrier stiffness. The observed nanomechanical properties in the NPC indicate the presence of a cohesive barrier to transport, and are quantitatively consistent with the presence of a central condensate of nuclear pore proteins in the NPC channel.

The NPC has been studied using a variety of biochemical and microscopy techniques, leading to a good understanding of its cytoplasmic ring structure and shape[2-5]. Superresolution optical microscopy has recently provided insight into the transient distributions of specifically labelled intrinsic (nuclear pore proteins; Nups) and extraneous (cargo) components, as well as nuclear transport receptors in the NPC[8-10]. However, the central channel still eludes detailed structural and nanomechanical characterization, because its intrinsically disordered nature is not amenable to approaches that are based on crystallography, and because its central location deep within the NPC structure has so far remained inaccessible to surface techniques such as atomic force microscopy (AFM). The nature of the selective barrier is therefore unknown, and it has been hypothesised that Nups act as a dynamic polymer brush[11-13], or form a partially[14] or predominantly cross-linked network (hydrogel)[15]. AFM has previously visualized the surface topography of fixed[16] and unfixed NPCs[17] (Fig. 1a) in isolated nuclear envelopes, which maintain physiological selectivity and rate of transport[18]. It has also been used to study recombinant Nups tethered in artificial configurations[13],[19] and their interactions with nuclear transport receptors[20]. Though subsurface AFM imaging and stiffness topography have been demonstrated on micron length scales[7],[21], it requires significant refinement to reveal nanometre-scale details of complex biomolecular machines such as the NPC.

To probe the organization and mechanics of Nups inside NPC channels from *Xenopus laevis* oocytes, we used high-aspect ratio, supersharp silicon tips, with a typical radius of 2 nm. This is significantly smaller than the NPC channel diameter (~50 nm, Fig. 1a and Supplementary Figs. 1-2) and approaches the ultimate ~1 nm diameter, cylindrical tip shape that could be achieved by using single-molecule, carbon-nanotube tips[22]. With these tips, we collected force curves that relate the force exerted on the AFM tip to the distance travelled by the tip towards and into the NPC. Curves were collected starting several tens of nanometres away from the cytoplasmic surface of the NPC down to an indentation of > 20 nm, which corresponds to more than 1/3 of the channel depth. This was repeated on a grid of points spanning the entire cytoplasmic surface of each NPC. The un-indented NPC surface topography was determined from the vertical (z) position where the force first surpassed the background noise (Fig. 1b). The data were subsequently symmetrized around the central axis of the NPC and converted into stiffness cross sections (Fig. 1c), where the local stiffness was defined as the force gradient $-\partial F(r, z)/\partial z$. The measured force and stiffness curves (Fig. 1d-e) described the nanomechanical properties of the NPC. The stiffness cross sections highlighted the presence of two distinct structural features within the NPC: a cytoplasmic ring structure (“rim”) and a central plug in the channel, which become more pronounced on averaging over larger numbers of NPCs and which are in good agreement with density plots obtained by cryoelectron microscopy[2-4] (Supplementary Fig. 2).

While the plug (also called transporter) structure appears a central feature to the NPC transport barrier, its nature and role in transport are unclear. It has been attributed to the intramolecular[23] and/or collective[24] structure of the Nups, as well as to cargos in transit[2-5]. To explore the biochemical nature of the central plug, we incubated isolated nuclei with Ran-/E-mix (see Methods) to activate the transport cycle *in vitro* and thus flush out cargos from NPCs before AFM analysis. In addition, we treated isolated nuclear envelopes with Benzonase to digest any remaining ribonucleoproteins (RNPs) trapped in the NPCs during transport. Fluorescence microscopy experiments confirmed the successful reactivation of the transport cycle (Fig. 2a), and a significant reduction of RNP complexes upon Ran-/E-mix and Benzonase treatments (Fig. 2b). This was further confirmed by quantification of the fluorescence signal (Fig. 2c-d) and Western blot of isolated nuclear envelopes for quantification of RNP K/J, a component of messenger RNPs, and of IBB-GFP, an exogenously added cargo (Fig. 2e). In AFM measurements, the central plug and stiffness cross sections of NPCs were not affected by removal of cargos, as demonstrated in stiffness cross sections and stiffness curves that represent data as in Fig. 1c and e, but averaged over several tens of NPCs (Fig. 2f). These features also persisted following removal of the nuclear basket (Supplementary Fig. 3). Furthermore, the force curves did not show any signature of entanglement of the AFM tip within the NPC channel or of irreversible deformation of the NPC (Supplementary Fig. 4a-c), which would lead to hysteresis between loading and unloading curves as we observed when indenting at forces significantly exceeding those used throughout this study (Supplementary Fig. 4d-f). We therefore conclude that the increased stiffness detected in the centre of the NPC is a distinctive feature of the transport barrier itself.

For selective transport, nuclear transport receptors overcome the barrier by binding to the Nups. The Ran-/E-mix treatment resulted in a partial removal of nuclear transport receptors from the NPCs (Supplementary Fig. 5), without significantly affecting the stiffness profile (Fig. 2f). We therefore decided to study how the addition of exogenous nuclear transport receptors[25,26] affected the NPC central channel by incubating NPCs with recombinant importin β for 10 minutes prior to AFM measurement (Fig. 2g). Incubation with 0.5 μM importin β produced a distinct swelling of the channel. It also resulted in a more homogeneous stiffness profile across the channel. This trend was confirmed by incubating with a higher (4.0 μM) importin β concentration (Supplementary Fig. 6). The AFM tip itself did not experience a significant attractive interaction with the Nups in the NPC channel (Supplementary Fig. 4), which would otherwise be observable as a negative force and/or characteristic dip in the force spectroscopy data. No such negative forces were observed in reconstituted configurations either[13,19], implying that electrostatic interactions between the negatively charged tip and positively charged Nups domains[27] were insufficient to overcome the transport barrier.

Experimentally, we thus observed a transport barrier that includes a central plug as an intrinsic component (Fig. 2f). This observation is in qualitative agreement with the prediction that Nup-coated nanopores can form a central, cohesive Nup condensate on increasing inter-Nups attractive forces[24,28], with Nups binding to other Nups that are anchored to diametrically opposite sites in the channel. Such behaviour may be further

enhanced by intramolecular heterogeneity[23]. Nuclear transport receptors have been predicted to bind on top of such a Nup condensate[29], leading to a swelling and homogenization of the upper layer of the transport channel as also observed experimentally (Fig. 2g). Furthermore, individual and averaged force and stiffness curves in the NPC central channel did not show the gradual, near-exponential increase that would have been expected for indentation against the steric forces in brush-like scenarios for the transport barrier. Instead, indentation models for gel-like, cohesive materials yielded good fits to our experimental data (Fig. 1e and Supplementary Fig. 7). The force curves also closely resembled data recorded on recombinant, cohesive Nups from the same organism[19] (Supplementary Fig. 8).

To test if the central stiffness within the NPC can be attributed to cohesive interactions between Nups, we designed a numerical simulation of AFM indentation in a nanopore of radius R = 25 nm, coated with 216 interacting polymers of a length corresponding to the average length of the disordered Nup domains in vertebrate NPCs (~161 nm) and consisting of chains of beads of 0.76 nm diameter (twice the contour length of a single amino acid), tethered over a vertical range of 30 nm, thus approximately mimicking the *Xenopus laevis* NPC channel[24,29]. This system was investigated for a range of interaction parameters in the immediate vicinity of a phase transition between a brush-like configuration with reduced polymer density at the centre of the channel (Fig. 3a), on one hand, and the formation of a central condensate (Fig. 3b), on the other[24].

For weakly interacting polymers (Fig. 3a), the calculated forces and stiffnesses (blue curves in Fig. 3c-d, and Supplementary Movie 1) were smaller than the experimental data by at least an order of magnitude. These calculated curves were also – even taking into account the difference in magnitude – much smoother, as expected for steric forces in a brush-scenario of the transport barrier. In contrast, quantitative agreement between theory and experiment was obtained for inter-polymer attractions that are just sufficiently strong to form a central condensate (Fig. 3b, black curves in Fig. 3c-d, and Supplementary Movie 2). This agreement was confirmed by inspection of individual, non-averaged experimental force curves, and was maintained on assuming a tip radius that was twice as large as the manufacturer's specification of 2 nm (Supplementary Figs. 9-10). In such a condensed state, active transport through the NPC would be facilitated by the presence of meta-stable open states in which the Nups are rearranged closer to their anchoring points at the channel wall[24]. We note that nuclear transport receptors have been proposed to act as intrinsic constituents of the NPC transport barrier[25,26], which in the scenario proposed here would imply assisting in the formation of a central Nup condensate and/or tuning it to allow its transient dissolution for selective transport[29].

In summary, we have carried out a nanomechanical study of the transport barrier in intact NPCs. Our results demonstrate that Nups form a cohesive, cross-linked polymer network in the NPC channel, resembling a hydrogel but showing significant variation in Nup density as a function of radial position in the channel. This conclusion is supported by the qualitative appearance of the stiffness topography and force/stiffness curves in the NPC, as well as by the quantitative agreement of the force/stiffness curves with an NPC model that postulates the presence of a marginally stable Nups condensate in the central channel. It suggests a

Europe PMC Funders Author Manuscripts

transport mechanism in which nuclear transport receptors modulate the effective inter-Nups interactions[25] and thus gate active transport of bound cargo as large as viruses[30], whereas passive transport remains prohibited for molecules larger than a few nanometres.

Methods

Preparation of nuclear envelopes

The preparation of *Xenopus laevis* oocytes, nuclei and nuclear envelopes was carried out as described previously[17] with the exception that coverslip substrates were incubated for 30 minutes with 0.1% (w/v) poly-L-lysine (Sigma-Aldrich, St. Louis, MO, USA) prior to adsorption of nuclear envelopes. Nuclear envelope samples were kept unfixed in a buffer containing 87mM KCl, 3mM NaCl, 1.5mM $CaCl_2$, 1mM $MgCl_2$, 10mM HEPES, pH 7.4, at all times.

Biochemical treatment and functional characterization

For the experiments presented in Fig. 2a-f, the isolated nuclei were incubated (Supplementary Fig. 11) twice with Ran-Mix (0.3μM Ran, 0.3μM GDP, 0.06μM NTF2, 0.03μM RanGAP, 4nM Ran BP1) and E-Mix (0.75mM ATP, 0.75mM GTP, 15mM creatinP, 0.075mM $Mg(OAC)_2$, 0.075mM DTT, 0.075mg/ml creatin kinase in HEPES/KOH pH 7.5) for 20 minutes each. Washings were performed in a nuclear isolation medium (NIM, 17mM NaCl, 90mM KCl, 10mM $MgCl_2$, 10mM TRIS, pH 7.4) supplemented with 1.5% Polyvynilpyrrolidone 40 (PVP). After each incubation, nuclei were washed by transferring them into new volume of NIM with 1.5% PVP. Isolated nuclear envelopes were incubated for 30 minutes with 25 units Benzonase®Nuclease (E1014-25KU, Sigma-Aldrich) per μl solution in NIM supplemented with 8% PVP. Control measurements were carried out on nuclei and nuclear envelopes exposed to the same procedure, but with the Ran-/E-mix and benzonase incubations replaced by incubations in NIM/1.5% PVP. After the Ran-/E-Mix and Benzonase treatment, the nuclear envelopes were incubated overnight at 4°C in NIM with 8% PVP. For subsequent AFM measurements, the buffer was changed to NIM without PVP. See Supplementary Information for further details on verifying the effectiveness of the procedure by confocal fluorescence microscopy and Western blotting.

Atomic force microscopy

The application of AFM to nuclear envelopes has been described in detail elsewhere[17]. We used MultiMode IV and VIII AFM systems (Bruker AXS, Santa Barbara, CA, USA). The larger-scale image (Fig. 1a) of a nuclear envelope was obtained in tapping mode using high-density carbon tips with nominal radius of 2-3 nm (Nanotools, Munich, Germany), grown on 0.1 N/m DNPS cantilevers (Bruker AXS). Force-spectroscopy was carried out with 0.1 N/m SHOCON-Super-Sharp tips (Applied Nanostructures, Santa Clara, CA, USA) with a nominal tip radius of 2 nm (guaranteed < 5nm) and a height-to-width aspect ratio better than 3.5:1. To minimize the risk of tip degradation, these were only employed (for simultaneous imaging and force spectroscopy of individual pores) once NPC-rich regions were located on the nuclear envelope by tapping-mode imaging with conventional tips, MSNL, Bruker AXS, and using optical images for position reference. With the supersharp tips, force-distance curves were recorded on coarse grids (16 × 16, 32 × 32 *xy* pixels) for the initial alignment of

Europe PMC Funders Author Manuscripts

the AFM tip to an NPC centre, and next recorded for 64 × 64 grids over areas of 200 × 200 nm^2, which typically included one NPC (~100 nm in diameter). A grid was completed in 10 minutes. Force curves were taken over a ramp size of 100 nm, indenting the sample up with a load rate of ~2 μm/sec, to a threshold force < 0.6 nN, such that entanglement and other hysteretic effects could be avoided (Supplementary Fig. 4). The panels with stiffness maps represent paired measurements, to minimize the effect of variations in sample preparation, calibration, and tip shape on the measurements. The results in Fig. 2f were based on roughly equal amounts of pores, analyzed by the same tips or tips from the same batch, from parallel preparations that only differed by the Ran-Benzonase treatment as described above. For the data in Fig. 2g, approximately equal amounts of pores on the same isolated nuclear envelopes were analyzed by the same tips for the control and importin-β measurements.

AFM data analysis

Force spectroscopy data were analyzed automatically using dedicated Mathematica (Wolfram Research, Champaign, IL, USA) programs. To reduce drift-related lateral deviations from the (approximately) rotational symmetry of the NPC, the rim shape of each NPC was manually traced in the images that were acquired, simultaneously with the force spectroscopy data, at maximum indentation force. Next, the measured force curves were grouped in ~4 nm wide shells that were concentric with the measured rim shape. Fig. 1b shows such shells of twice that size, overlaid with a surface plot of an NPC after Gaussian filtering ($\sigma = 2$ pixels). The smallest, inner shell provides the data for $r = 0$, the shell at the pore rim the data for $r = R$, etc.

For each force curve, the contact point (“true”, unindented height) between tip and sample was determined from the best fit that was achieved by assuming a constant force for the baseline and a constant force gradient over the shortest detectable range over which the data significantly deviated (by at least 2 standard deviations) from the baseline noise. Baselines were checked to be flat and free of pronounced features that may point to anomalous adhesion effects. Curves were excluded from the analysis if this was not the case (~10% of the curves, randomly distributed over the sample surface). The measured force was plotted against the tip-sample separation, corrected for cantilever deflection. The stiffness ($-\partial F/\partial z$) was obtained by taking the numerical derivative of the force curves after applying a Gaussian filter with $\sigma = 1$ nm. This is equivalent to earlier AFM stiffness topography approaches[7], except for a model-dependent prefactor that only depends on the indentation depth (see Supplementary Information); the resulting stiffness maps should be regarded as qualitative and spatially convolved representations of the underlying local elastic properties.

To reduce the effect of vertical (scanner and cantilever) drift and of unevenness of the supported nuclear envelopes, all force curves in a shell were shifted in z to align their contact points, and subsequently averaged. The shell-averaged true height was taken as the contact point for the shell-averaged force curve. Data were only considered for the z range where at least 70% of the to-be-averaged curves contained data points. The membrane adjacent to the NPC ($r = 2R$) was taken as a height reference ($z = 0$). The whole procedure was tested by digitally generating model curves with noise and subsequently analysing these using the same routines as those applied to the experimental data (Supplementary Fig. 12).

In an alternative analysis that confirmed the conclusions presented here, the individual force curves were fitted with a Hertzian contact model, yielding unindented topography and values for an effective bulk elastic modulus (Supplementary Figs. 13-15).

Modelling

The polymer model (Fig. 3 and Supplementary Movies 1 and 2) relies on a density functional theory approach that minimizes the free energy by varying a polymer density that is rotationally symmetric around the vertical axis, as described in detail elsewhere[24]. For calculating force and stiffness curves, this model was expanded by including the full AFM tip shape as a strongly repulsive, short-range external potential. From the free energy of the system as a function of tip position, the force and stiffness curves were obtained by subsequent differentiations.

Supplementary Material

Refer to Web version on PubMed Central for supplementary material.

Acknowledgements

We thank H. Oberleithner for the use of lab facilities, P. Vergani for assistance with the preparation of *Xenopus laevis* oocytes; D. Görlich for the expression plasmids for importin β and Ran-mix; S. Frey for Rch1-IBB-MBP-GFP protein; R.P. Richter for providing the data represented in Supplementary Fig. 8; J. Grech for the electron microscopy image in Fig. 1a; M. Goldberg for the protocol for removal of the nuclear basket from the NPCs; J. Bailey and A.H. Harker for support in initializing the modelling work; R. Thorogate for assistance with the confocal microscopy measurements; C. Leung for assistance in formatting the figures; and T. Duke (deceased) and G. Aeppli for proofreading the manuscript. This work was partially funded by the European Molecular Biology Organization (ALTF 757-2008 to A.K.), the Kazakh Ministry of Education and Science (A.B.), the Sackler Foundation (D.O.), the UK Biotechnology and Biological Sciences Research Council (BB/G011729/1 to B.W.H.) and the Wellcome Trust (083810/Z/07/Z to A.F.). G.C. is a Royal Society University Research Fellow.

References

1. Mohr D, Frey S, Fischer T, Güttler T, Görlich D. Characterisation of the passive permeability barrier of nuclear pore complexes. EMBO J. 2009; 28:2541–2553. [PubMed: 19680228]
2. Fahrenkrog B, Aebi U. The nuclear pore complex: nucleocytoplasmic transport and beyond. Nat. Rev. Mol. Cell Biol. 2003; 4:757–766. [PubMed: 14570049]
3. Alber F, et al. The molecular architecture of the nuclear pore complex. Nature. 2007; 450:695–701. [PubMed: 18046406]
4. Beck M, Lucic V, Forster F, Baumeister W, Medalia O. Snapshots of nuclear pore complexes in action taken by cryoelectron tomography. Nature. 2007; 449:611–615. [PubMed: 17851530]
5. Hoelz A, Debler EW, Blobel G. Structure of the nuclear pore complex. Annu. Rev. Biochem. 2011; 80:613–643. [PubMed: 21495847]
6. Tetenbaum-Novatt J, Rout MP. The mechanism of nucleocytoplasmic transport through the nuclear pore complex. Cold Spring Harb. Symp. Quant. Biol. 2011; 75:567–584. [PubMed: 21447814]
7. Roduit C, et al. Stiffness tomography by atomic force microscopy. Biophys. J. 2009; 97:674–677. [PubMed: 19619482]
8. Adams RL, Wente SR. Uncovering nuclear pore complexity with innovation. Cell. 2013; 152:1218–1221. [PubMed: 23498931]
9. Lowe AR, et al. Selectivity mechanism of the nuclear pore complex characterized by single cargo tracking. Nature. 2010; 467:600–603. [PubMed: 20811366]
10. Goryaynov A, Ma J, Yang W. Single-molecule studies of nucleocytoplasmic transport: from one dimension to three dimensions. Integr. Biol. (Camb.). 2012; 4:10–21. [PubMed: 22020388]

11. Macara IG. Transport into and out of the nucleus. Microbiol. Mol. Biol. Rev. 2001; 65:570–594. [PubMed: 11729264]
12. Rout MP, Aitchison JD, Magnasco MO, Chait BT. Virtual gating and nuclear transport: the hole picture. Trends Cell Biol. 2003; 13:622–628. [PubMed: 14624840]
13. Lim RY, et al. Nanomechanical basis of selective gating by the nuclear pore complex. Science. 2007; 318:640–643. [PubMed: 17916694]
14. Patel SS, Belmont BJ, Sante JM, Rexach MF. Natively unfolded nucleoporins gate protein diffusion across the nuclear pore complex. Cell. 2007; 129:83–96. [PubMed: 17418788]
15. Frey S, Görlich D. A saturated FG-repeat hydrogel can reproduce the permeability properties of nuclear pore complexes. Cell. 2007; 130:512–523. [PubMed: 17693259]
16. Jäggi RD, et al. Modulation of nuclear pore topology by transport modifiers. Biophys. J. 2003; 84:665–670. [PubMed: 12524319]
17. Kramer A, et al. Apoptosis leads to a degradation of vital components of active nuclear transport and a dissociation of the nuclear lamina. Proc. Natl. Acad. Sci. U.S.A. 2008; 105:11236–11241. [PubMed: 18678902]
18. Keminer O, Siebrasse JP, Zerf K, Peters R. Optical recording of signal-mediated protein transport through single nuclear pore complexes. Proc. Natl Acad. Sci. USA. 1999; 96:11842–11847. [PubMed: 10518538]
19. Eisele NB, Labokha AA, Frey S, Görlich D, Richter RP. Cohesiveness tunes assembly and morphology of FG nucleoporin domain meshworks - Implications for nuclear pore permeability. Biophys. J. 2013; 105:1860–1870. [PubMed: 24138862]
20. Rangl M, et al. Single-molecule analysis of the recognition forces underlying nucleo-cytoplasmic transport. Angew. Chem. Int. Ed. 2013; 52:10356–10359.
21. Tetard L, Passian A, Thundat T. New modes for subsurface atomic force microscopy through nanomechanical coupling. Nature Nanotech. 2010; 5:105–109.
22. Wilson NR, Macpherson JV. Carbon nanotube tips for atomic force microscopy. Nature Nanotech. 2009; 4:483–491.
23. Yamada J, et al. A bimodal distribution of two distinct categories of intrinsically disordered structures with separate functions in FG nucleoporins. Mol. Cell Proteomics. 2010; 9:2205–2224. [PubMed: 20368288]
24. Osmanović D, et al. Bistable collective behavior of polymers tethered in a nanopore. Phys. Rev. E. 2012; 85:061917.
25. Schoch RL, Kapinos LE, Lim RY. Nuclear transport receptor binding avidity triggers a self-healing collapse transition in FG-nucleoporin molecular brushes. Proc. Natl Acad. Sci. USA. 2012; 109:16911–16916. [PubMed: 23043112]
26. Jovanovic-Talisman T, et al. Artificial nanopores that mimic the transport selectivity of the nuclear pore complex. Nature. 2009; 457:1023–1027. [PubMed: 19098896]
27. Tagliazucchi M, Peleg O, Kröger M, Rabin Y, Szleifer I. Effect of charge, hydrophobicity, and sequence of nucleoporins on the translocation of model particles through the nuclear pore complex. Proc. Natl Acad. Sci. USA. 2013; 110:3363–3368. [PubMed: 23404701]
28. Peleg O, Tagliazucchi M, Kröger M, Rabin Y, Szleifer I. Morphology control of hairy nanopores. ACS Nano. 2011; 5:4737–4747. [PubMed: 21524134]
29. Osmanović D, Ford IJ, Hoogenboom BW. Model inspired by nuclear pore complex suggests possible roles for nuclear transport receptors in determining its structure. Biophys. J. 2013; 105:2781–2789. [PubMed: 24359750]
30. Zaitseva L, Myers R, Fassati A. tRNAs promote nuclear import of HIV-1 intracellular reverse transcription complexes. PLoS Biol. 2006; 4:e332. [PubMed: 17020411]

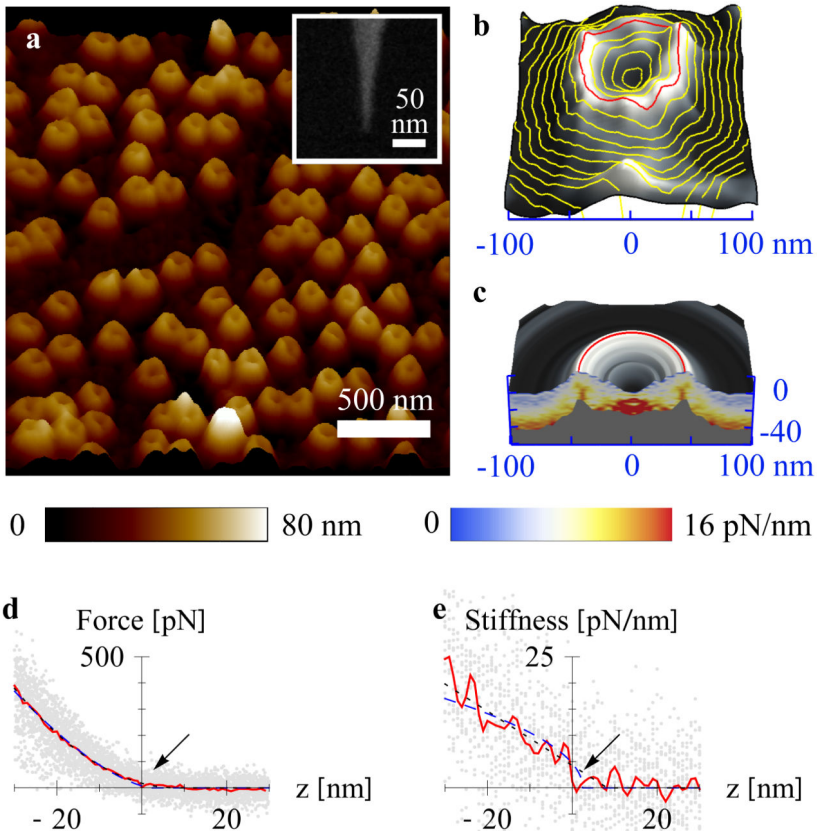

Figure 1. NPCs imaged and probed by AFM

a, Tapping-mode AFM image of the cytoplasmic side of an isolated nuclear envelope. Inset: Electron microscopy image of a supersharp AFM tip. **b**, AFM-image representing the un-indented cytoplasmic surface of a single NPC, reconstructed from a force spectroscopy measurement. The red line marks the cytoplasmic ring structure, and yellow lines define shells that are concentric with it. **c**, Rotationally symmetrized surface (grey scale) based on the image in b. The blue-to-red colour scale represents a vertical cross section showing the rotationally averaged local stiffness $-\partial F(r, z)/\partial z$ that was experienced by the probe on and in the NPC. The plain grey area denotes indentation depths for which insufficient force data were available. **d**, Force (grey dots) as a function of tip-sample separation for lateral positions with radii $r < 0.2\ R$ inside the NPC, where R is the average radius of the cytoplasmatic ring. The red curve is the average of the force data, and the arrow indicates the contact point. The blue and black dashed lines correspond to fits with indentation models for a spherical and a conical tip, respectively (see Supplementary Eqs. 2-3). **e**, Stiffness as a function of tip-sample separation for radial positions $r < 0.2\ R$ inside the NPC.

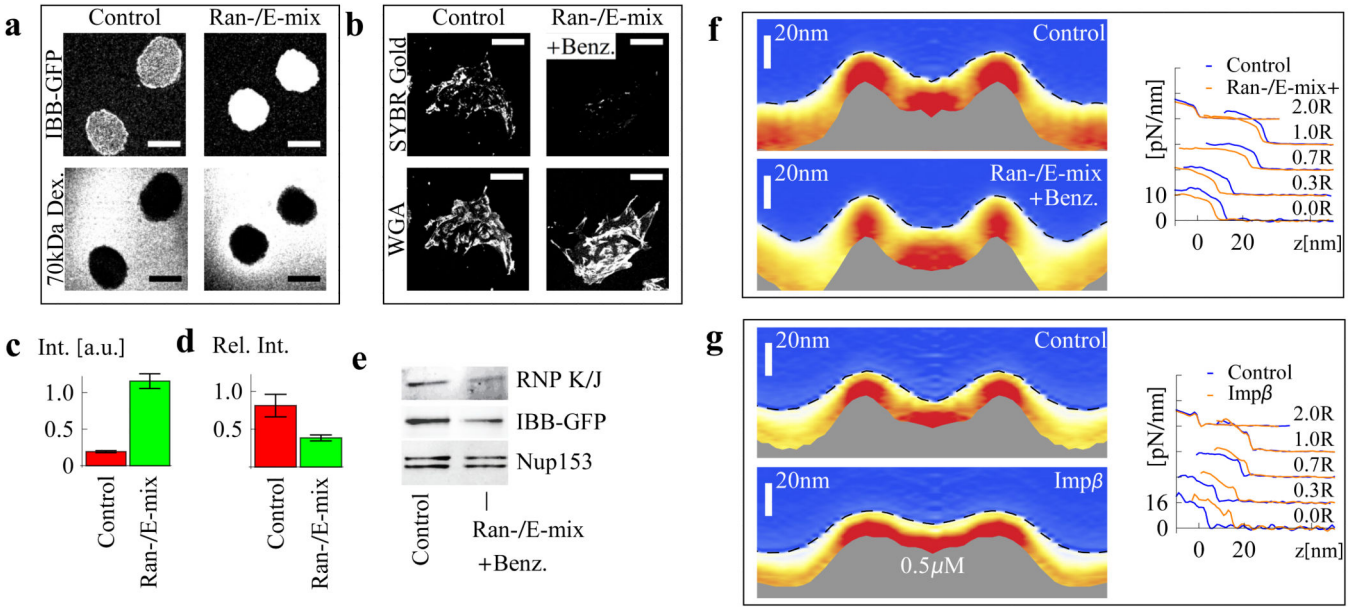

Figure 2. Structure and nanomechanical properties of NPCs

a, Confocal microscopy of isolated *Xenopus laevis* nuclei washed in buffer without (Control) or with Ran-/E-mix. Rch1-IBB-MBP-GFP ("IBB-GFP") was added to the nuclei before treatment, and accumulated in the nuclei upon addition of Ran-/E-mix, while 70 kDa dextran remained excluded, indicating that the nuclei were intact. **b**, Confocal microscopy images of nuclear envelopes isolated from nuclei washed in buffer without (Control) or with Ran-/E-mix, and (the nuclear envelopes) subsequently exposed to Benzonase ("Benz."). Nucleic acids were labelled with SYBR Gold, and fluorescent wheat germ agglutinin (WGA) was used to label NPCs. Scale bars in a, b: 400 μm. **c**, Quantification of IBB-GFP fluorescent signal in the nuclei (n = 15 for control and n = 16 for Ran-/E-mix data, with standard errors of the mean). **d**, Quantification of the SYBR Gold fluorescent signal at the nuclear envelopes, normalized to the WGA signal (n = 11 for control and n = 10 for Ran-/E-mix+Benz. data, with standard errors of the mean) for samples treated as described in a, b. **e**, Western blot from isolated nuclear envelopes showing a reduction of RNP K/J and IBB-GFP following Ran-/E-mix and Benzonase treatment; Nup153 was used as a loading control. **f**, Averaged stiffness cross sections of NPCs following washes without (Control) and with Ran-/E-mix and Benzonase. Black, dashed lines indicate the averaged profiles of the un-indented NPC surface. The same data are also shown as stiffness (in pN/nm) versus vertical position (z), for different radial positions, offset for clarity. **g**, Averaged stiffness cross sections of NPCs measured before (Control) and after 10 minutes incubation of the isolated nuclear envelopes with 0.5 μM importin β (Impβ). Number of NPCs in each data set: n = 33 (f, Control); n = 36 (f, Ran-/E-mix+Benz.); n = 35 (g, Control); n = 40 (g, Impβ). Colour scale: 0-10 pN/nm (f); 0-16 pN/nm (g).

Europe PMC Funders Author Manuscripts

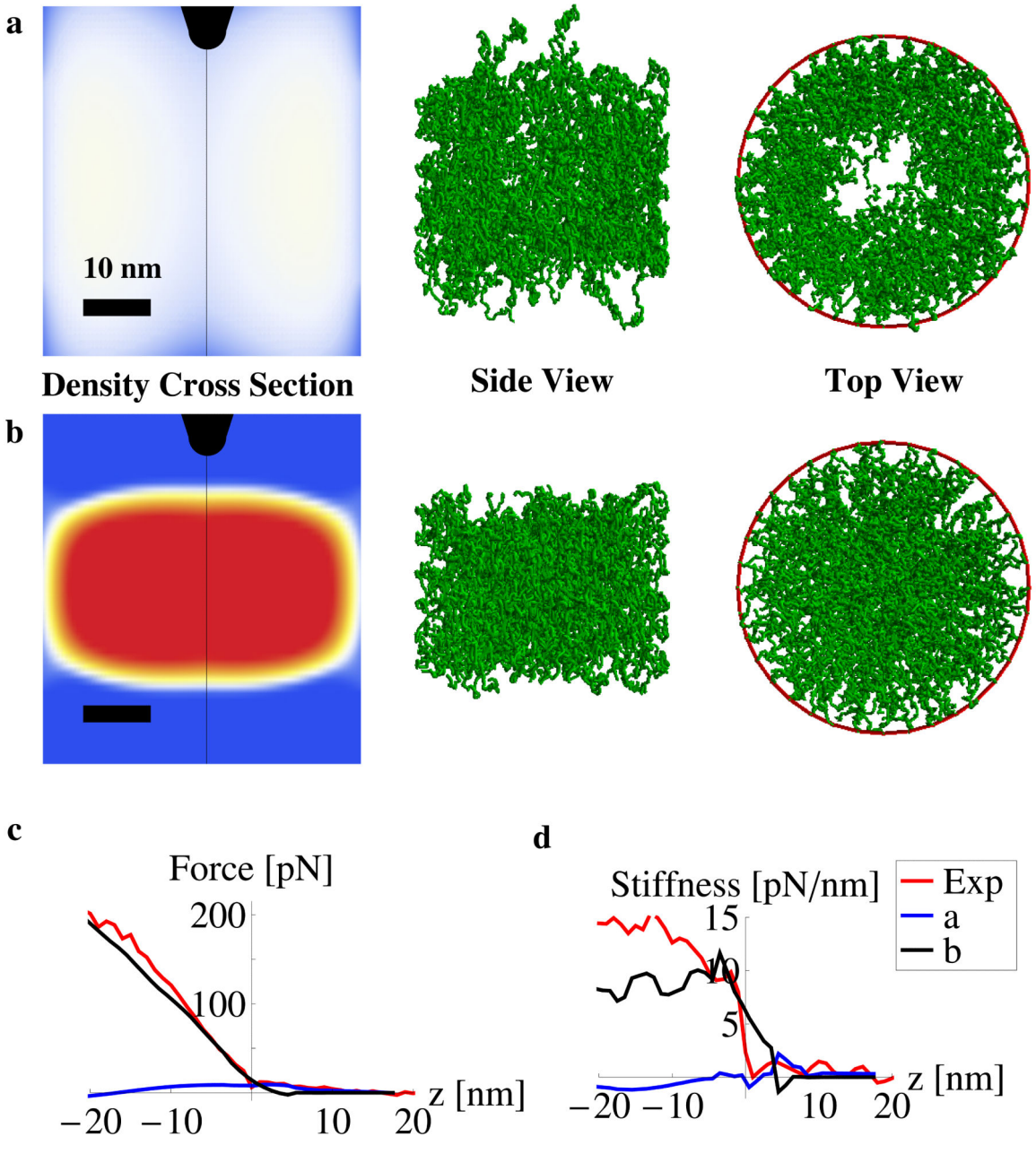

Figure 3. Nups modelled as interacting polymers in a cylindrical geometry

a-b, Left column: Density cross sections for interacting polymers (see text) in a nanopore configuration that approximately mimics the NPC channel geometry[29] (with AFM tip in black). Results are shown for interpolymer bead-bead pair attractions with decay length 1 nm and strengths of 0.02 and 0.05 k_BT for a and b, respectively[24]. Centre and right columns: Side and top views of the approximate polymer configurations corresponding to the calculated polymer density profiles. **c-d**, Calculated force and stiffness curves for a supersharp AFM tip indenting the polymer assemblies as displayed in a (blue curve) and b

(black curve), compared to the experimental curves averaged from control data (red, “Exp”, n = 107 NPCs). z = 0 refers to the contact point in the experimental data; the z offset of the theoretical data was adjusted to achieve the best match to the experimental data.

Europe PMC Funders Author Manuscripts